On a geometrically nonlinear incremental formulation for the modeling of 3D concrete printing

Boumediene Nedjar

On a geometrically nonlinear incremental formulation for the modelling of 3D concrete printing

B. Nedjar[a,*]

[a] *Université Gustave Eiffel, MAST/EMGCU,*
5 Boulevard Descartes, 77454 Marne-la-Vallée cedex 2, France

Abstract

Of interest in this paper is a modelling framework when constitutive relations are given in incremental form. This is particularly true for aging concretes due to hydration. Furthermore, having in mind applications to 3D concrete printing, geometrical nonlinearities must be accounted for due to the soft nature of the fresh material. The kinematics must then be adapted adequately for a theoretically sound formulation. For this, the multiplicative split is chosen here for the deformation gradient into its known part at an earlier time and the relative deformation gradient. From the geometric point of view, this gives rise to an intermediate configuration on which incremental constitutive relations can be ideally defined prior to be transported back to the reference configuration for a Lagrangian formulation. Model examples are given for the purpose of demonstration and a set of simulations illustrate the effectiveness of the proposed framework.

Keywords: Additive manufacturing, Large deformations, Incremental formulation, Multiplicative kinematics, Incremental finite strain elasticity

1. Introduction

The emerging additive manufacturing technology is gaining more and more interest. Among the fields of applications, the challenging 3D concrete printing is nowadays receiving considerable attention in civil engineering due to the potential applications including, for instance, connection elements, structural elements, up to complete buildings, see for example [1, 2, 3] among others.

During the 3D printing, for instance through the widely used layer-by-layer extrusion technique, the concrete is still fresh. Its buildability is largely influenced by the early age mechanical properties and rheology, e.g. see for example [4, 5, 6]. These informations are in turn important for efficient theoretical modelling that will feed numerical tools for predictive simulations and optimal design. Recently, maybe the most important numerical model is the one proposed in [7, 8] where a finite element analysis has been conducted with time-dependent linear elasticity in combination with time-dependent Mohr-Coulomb failure criterion. The results reported by the authors are promising and seem in close agreement with the experimental results. However, the particularity of fresh concrete is its aging because of the hydration process, e.g. [9]. Consequently, the only possible way to express the constitutive relation would be in incremental form and not in a direct form, e.g. see for instance [10, 11]. This important restriction will be adopted in this work as well.

In addition, as fresh concrete must carry its self-weight with the absence of any confining formwork, a predictive theory must be able to capture eventual buckling mechanisms, e.g. [12, 13]. A geometrically nonlinear formulation will then be a priori adopted. Moreover, a finite strain approach is necessary for big area additive manufacturing where the cross-sectional shape can vary substantially, e.g. see [14]. However, keeping in mind that incremental constitutive relations will be used, the kinematics must be adapted adequately. Herein, we adopt the multiplicative decomposition of the deformation gradient into its known part at an earlier time and the rela-

*Corresponding author, phone: +33 1 81 66 84 16
Email address: boumediene.nedjar@univ-eiffel.fr (B. Nedjar)

tive deformation gradient with respect to the configuration at that time. This gives rise to an intermediate configuration on which incremental constitutive relations for the stresses can be well defined. Two model examples are proposed in this work that are inspired by known hyperelastic models widely used in the literature: a Saint-Venant-like model and a compressible neoHooke-like model, e.g. see [15, 16, 17]. From the theoretical point of view, it is very important to notice that in this formulation, one cannot speak of hyperelastic nor elastic models, but only of hypoelastic ones. Futhermore, even if the material properties of an aging concrete basically depend on time-dependent hydration degree and time-dependent temperature, in this work we only consider their direct dependence upon time focusing on the purely mechanical aspects. The topics of thermo-hydric couplings, and more, will soon be addressed in future contributions. To go further, the mechanical equilibrium equation is adapted as well due to the same reasons. Herein, a Lagrangian formulation is adopted: the chosen incremental constitutive relations must then be pull-back from the *known* intermediate configuration to the reference (initial) configuration. We show that the above kinematics is well suited for this transport procedure.

Notations: Throughout the paper, bold face characters refer to second- and fourth-order tensorial quantities. The notation $(\boldsymbol{.})^T$ is used for the transpose operator, and the double dot symbol ':' is used for double tensor contraction, i.e. for any second-order tensors $\boldsymbol{A}$ and $\boldsymbol{B}$, $\boldsymbol{A}\!:\!\boldsymbol{B} = \mathrm{tr}[\boldsymbol{A}\boldsymbol{B}^T] = A_{ij}B_{ij}$ where, unless specified, summation over repeated indices is always assumed. The notation $\otimes$ stands for the tensorial product, i.e. in components, one has $(\boldsymbol{A}\otimes\boldsymbol{B})_{ijkl} = A_{ij}B_{kl}$.

2. Basic equations

The formulation is a priori developed within the finite strain range because of the soft nature of the fresh printed concrete. We give the main governing equations where we first state the balance equation that is adapted to an incremental form of the constitutive relations, then we discuss the kinematics that best matches this particularity. Model examples will be addressed next in Section 3.

2.1. Mechanical balance

When undeformed and unstressed, the body occupies the reference configuration $\mathcal{B}_0$ with boundary $\partial\mathcal{B}_0$. We identify a material particle by its position vector $\boldsymbol{X} \in \mathcal{B}_0$ and we trace its motion by its current position in the spatial configuration $\mathcal{B}_t$ at time t as $\boldsymbol{x} = \boldsymbol{\varphi}_t(\boldsymbol{X}) \in \mathcal{B}_t$ where $\boldsymbol{\varphi}_t(\boldsymbol{.}) \equiv \boldsymbol{\varphi}(\boldsymbol{.}, t)$ denotes the deformation map at time t within a time interval $[0, T]$. The deformation gradient is defined as $\boldsymbol{F} \equiv \boldsymbol{F}_t = \nabla_{\boldsymbol{X}}\boldsymbol{\varphi}$ where $\nabla_{\boldsymbol{X}}(\boldsymbol{.})$ is the material gradient operator with respect to $\boldsymbol{X}$. The Jacobian of the transformation is given by the determinant $J = \det[\boldsymbol{F}]$ with the standard convention $J > 0$. With respect to the initial configuration, the mechanical equilibrium is equivalently given by the following weak form in terms of the first Piola-Kirchhoff stress tensor $\boldsymbol{P} \equiv \boldsymbol{P}_t$:

$$\int_{\mathcal{B}_0} \boldsymbol{P} : \nabla_{\boldsymbol{X}}(\delta\boldsymbol{\varphi})\ \mathrm{d}V = \int_{\mathcal{B}_0} \rho_0\bar{\boldsymbol{b}}.\delta\boldsymbol{\varphi}\ \mathrm{d}V\ , \quad (1)$$

which must hold for any admissible deformation variation $\delta\boldsymbol{\varphi}$. Here the vector $\rho_0\bar{\boldsymbol{b}}$ defines the body force due to gravitation, i.e. the self-weight, where ρ_0 is the initial density. However, as the first Piola-Kirchhoff stress tensor $\boldsymbol{P}$ is in general non-symmetric, it is better to use the second Piola-Kirchhoff stress tensor $\boldsymbol{S}$ that is symmetric. They are related by $\boldsymbol{P} = \boldsymbol{F}\boldsymbol{S}$ that when replaced into (1), this gives:

$$\int_{\mathcal{B}_0} \boldsymbol{S} : \boldsymbol{F}^T\nabla_{\boldsymbol{X}}(\delta\boldsymbol{\varphi})\ \mathrm{d}V = \int_{\mathcal{B}_0} \rho_0\bar{\boldsymbol{b}}.\delta\boldsymbol{\varphi}\ \mathrm{d}V\ . \quad (2)$$

Now a constituve relation must be appended. Here the particularity is that the stress tensor is *not* directly linked to a strain measure, i.e. for instance as for a hyperlastic material through a strain energy function. Within a typical time interval $[t_n, t_{n+1}]$, we make the following choice for the stress tensor $\boldsymbol{S} \equiv \boldsymbol{S}_t$:

$$\boldsymbol{S} = \boldsymbol{S}_n + \Delta\boldsymbol{S}\ , \quad (3)$$

where $\boldsymbol{S}_n$ is the *known* second-Piola Kirchhoff stress tensor at time t_n, and $\Delta\boldsymbol{S} \equiv \Delta\boldsymbol{S}_t$ is the second Piola-Kirchhoff stress tensor increment at the actual time $t \in [t_n, t_{n+1}]$. Thus, when replacing (3) into (2), we end up with the basic balance equation to be solved in our formulation:

$$\int_{\mathcal{B}_0} \boldsymbol{F}(\boldsymbol{S}_n + \Delta\boldsymbol{S}) : \nabla_{\boldsymbol{X}}(\delta\boldsymbol{\varphi})\ \mathrm{d}V = \int_{\mathcal{B}_0} \rho_0\bar{\boldsymbol{b}}.\delta\boldsymbol{\varphi}\ \mathrm{d}V. \quad (4)$$

Notice that in this latter: (i) the deformation gradient $\boldsymbol{F}$ is the actual one at time t, (ii) the gravitation force does not need to be incremented, and (iii) the equation is valid for any *incremental* constitutive relation through the definition of $\Delta\boldsymbol{S}$.

2.2. Linearization of the mechanical balance

The incremental form (4) is highly nonlinear, on the one hand because of the geometrical nonlinearities, and on the other hand because of nonlinearities stemming from the incremental constitutive relations. Its linearization is then necessary if the problem is to be solved numerically when using a Newton-type method.

As customary, we denote by $\boldsymbol{u}(\boldsymbol{X})$ the displacement of the particle $\boldsymbol{X} \in \mathcal{B}_0$ such that $\boldsymbol{\varphi}(\boldsymbol{X}) = \boldsymbol{X} + \boldsymbol{u}(\boldsymbol{X})$. The linearization of Eq. (4) is computed at a deformation map $\overline{\boldsymbol{\varphi}} = \boldsymbol{\varphi}_n + \Delta\boldsymbol{u}$ where $\boldsymbol{\varphi}_n$ is the known deformation at time t_n and $\Delta\boldsymbol{u}$ is the iteratively updated displacement increment. Following standard procedures, e.g. for instance [15, 16, 18], one obtains:

$$\begin{aligned} &\int_{\mathcal{B}_0} \Big\{ \nabla_{\boldsymbol{X}}(\Delta\boldsymbol{u})\,(\boldsymbol{S}_n + \Delta\boldsymbol{S}) : \nabla_{\boldsymbol{X}}(\delta\boldsymbol{\varphi}) \\ &\qquad + \delta\boldsymbol{E} : \overline{\boldsymbol{\Xi}} : \Delta\boldsymbol{E} \Big\}\, \mathrm{d}V \\ &= \int_{\mathcal{B}_0} \Big\{ \rho_0 \bar{\boldsymbol{b}}.\delta\boldsymbol{\varphi} \;-\; (\boldsymbol{S}_n + \Delta\boldsymbol{S}) : \delta\boldsymbol{E} \Big\}\, \mathrm{d}V \;, \end{aligned} \tag{5}$$

where $\delta\boldsymbol{E}$ and $\Delta\boldsymbol{E}$ are respectively the variation and the linearization of the Green-Lagrange strain tensor[1] given by,

$$\begin{aligned} \delta\boldsymbol{E} &= \frac{1}{2}\Big\{ \boldsymbol{F}^T \nabla_{\boldsymbol{X}}(\delta\boldsymbol{\varphi}) + \nabla^T_{\boldsymbol{X}}(\delta\boldsymbol{\varphi})\boldsymbol{F} \Big\} \;, \\ \Delta\boldsymbol{E} &= \frac{1}{2}\Big\{ \boldsymbol{F}^T \nabla_{\boldsymbol{X}}(\Delta\boldsymbol{u}) + \nabla^T_{\boldsymbol{X}}(\Delta\boldsymbol{u})\boldsymbol{F} \Big\} \;, \end{aligned} \tag{6}$$

and where $\overline{\boldsymbol{\Xi}}$ is the fourth-order tangent modulus that depends on the incremental constitutive relation, see below in Section 3. The stress tensor increment $\Delta\boldsymbol{S}$ and the tangent modulus $\overline{\boldsymbol{\Xi}}$ have to be evaluated at $\overline{\boldsymbol{\varphi}}$.

2.3. Kinematic assumption and structure of the incremental constitutive relations

At this point a natural question arises: How incremental finite strain constitutive relations should look like? To answer to this question, we first have to make a kinematical choice. Let $\boldsymbol{F}_n$ be the deformation gradient at time t_n, the actual deformation gradient $\boldsymbol{F}$ at time $t \in [t_n, t_{n+1}]$ is given by the following multiplicative decomposition, e.g. [19, 20],

$$\boldsymbol{F} = \tilde{\boldsymbol{f}}\boldsymbol{F}_n \;, \tag{7}$$

where $\tilde{\boldsymbol{f}} \equiv \tilde{\boldsymbol{f}}_t$ is the relative deformation gradient, see Fig. 1 for an illustration. This latter is the first ingredient from which one can define the relative right Cauchy-Green tensor $\tilde{\boldsymbol{c}}$ with respect to the intermediate configuration $\boldsymbol{\varphi}_n$ as,

$$\tilde{\boldsymbol{c}} = \tilde{\boldsymbol{f}}^T \tilde{\boldsymbol{f}} \;. \tag{8}$$

For later use, one has the following useful relation connecting $\tilde{\boldsymbol{c}}$ with the right Cauchy-Green tensor $\boldsymbol{C} = \boldsymbol{F}^T\boldsymbol{F}$:

$$\tilde{\boldsymbol{c}} = \boldsymbol{F}_n^{-T} \boldsymbol{C} \boldsymbol{F}_n^{-1} \;. \tag{9}$$

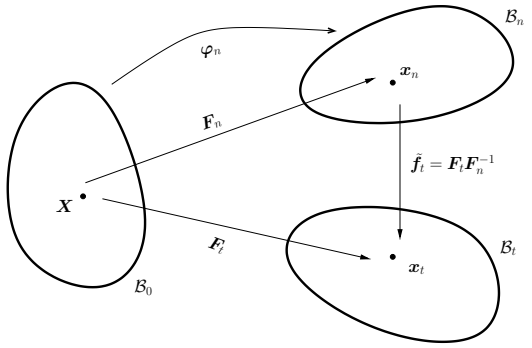

Figure 1: Total and relative deformation gradients connecting configurations $\mathcal{B}_0$, $\mathcal{B}_n$ and $\mathcal{B} \equiv \mathcal{B}_t$.

The second ingredient is that the incremental stress can be first defined on the *intermediate* configuration $\boldsymbol{\varphi}_n$ where we define the second Piola-Kirchhoff-type stress tensor increment that we denote here by $\tilde{\boldsymbol{s}}$, and with the form,

$$\tilde{\boldsymbol{s}} \;\equiv\; \tilde{\boldsymbol{s}}(\tilde{\boldsymbol{c}}) \;. \tag{10}$$

We then transform this latter back to the reference configuration by appropriate tensorial procedure:

$$\Delta\boldsymbol{S} = \boldsymbol{F}_n^{-1}\, \tilde{\boldsymbol{s}}\, \boldsymbol{F}_n^{-T} \;. \tag{11}$$

In a geometric context, one refers to (11) as a pull-back, e.g. [21]. The result (11) is to be replaced into the balance equation (4). Except for a Saint-Venant-like model, see below in Section 3.2, the procedure (10)-(11) is well adapted for incremental models inspired from many classical hyperelastic ones, for instance, neoHooke, Mooney-Rivlin, classical Hencky, exponentiated Henchy, or even Ogden like models, e.g. [15, 18].

[1] We recall the definition of the Green-Lagrange strain tensor: $\boldsymbol{E} = \frac{1}{2}\{\boldsymbol{C} - \boldsymbol{1}\}$, where $\boldsymbol{C} = \boldsymbol{F}^T\boldsymbol{F}$ is the right Cauchy-Green tensor and $\boldsymbol{1}$ is the second-order identity tensor.

3. Model examples

In this section two model examples of incremental constitutive relations are given. For the sake of clarity, focus is made on the purely mechanical aspects where thermo-hydric couplings are not considered. For both models, the expression of the second Piola-Kirchhoff stress tensor increment $\Delta\boldsymbol{S}$ and of the tangent modulus $\overline{\overline{\boldsymbol{\Xi}}}$ are given that must be used within a numerical resolution procedure.

3.1. A compressible neoHooke-like model

Among the many possible model examples, we choose perhaps one of the most popular in its hyperelastic version. Herein, one does not speaks of strain energy function because of the *hypoelastic* character of the constitutive relation, i.e. incremental form. Inspired by a compressible version of the neoHooke model, let postulate the following relation for the second Piola-Kirchhoff-type stress tensor increment with respect to the configuration $\boldsymbol{\varphi}_n$ in terms of the relative right Cauchy-Green tensor[2]:

$$\tilde{\boldsymbol{s}} \;=\; \lambda(t)\,\log[\tilde{j}]\,\tilde{\boldsymbol{c}}^{-1} \;+\; \mu(t)\,\big(\boldsymbol{1}-\tilde{\boldsymbol{c}}^{-1}\big)\;, \qquad (12)$$

where $\log[\centerdot]$ is the natural logarithm function and $\tilde{j}$ is the jacobian of the relative deformation gradient: $\tilde{j}=\det[\tilde{\boldsymbol{f}}]$. Here and in all what follows, $\boldsymbol{1}$ is the second-order identity tensor with components δ_{ij} (δ_{ij} being the Kronecker delta). The time-dependent parameters $\lambda(t)$ and $\mu(t)$ are Lamé-like coefficients within the asymptotic infinitesimal limit. They are related to the time-dependent Young's modulus $E(t)$ and the Poisson's ratio $\nu(t)$ as:

$$\lambda(t)=\frac{\nu(t)E(t)}{(1+\nu(t))(1-2\nu(t))} \quad \mu(t)=\frac{E(t)}{2(1+\nu(t))}\;. \qquad (13)$$

Now using the pull-back relation (11), we end-up with the following expression for the second Piola-Kirchhoff stress increment:

$$\begin{aligned}\Delta\boldsymbol{S} \;&=\; \lambda(t)\Big(\log[J]-\log[J_n]\Big)\,\boldsymbol{C}^{-1}\\ &+\; \mu(t)\Big(\boldsymbol{C}_n^{-1}-\boldsymbol{C}^{-1}\Big)\;,\end{aligned} \qquad (14)$$

where $J_n=\det[\boldsymbol{F}_n]$, $\boldsymbol{C}_n=\boldsymbol{F}_n^T\boldsymbol{F}_n$, and use has been made of the relation $J=\tilde{j}J_n$. The fourth-order tangent modulus is obtained by computing the derivative with respect to the right Cauchy-Green tensor as,

$$\begin{aligned}\overline{\overline{\boldsymbol{\Xi}}} \;&=\; \frac{\partial\Delta\boldsymbol{S}}{\partial\boldsymbol{E}}\equiv 2\,\frac{\partial\Delta\boldsymbol{S}}{\partial\boldsymbol{C}}\\ &=\; \lambda(t)\;\boldsymbol{C}^{-1}\otimes\boldsymbol{C}^{-1}\\ &+\; 2\Big(\mu(t)-\lambda(t)\,\log\left[\frac{J}{J_n}\right]\Big)\;\boldsymbol{I}_{\boldsymbol{C}^{-1}}\;,\end{aligned} \qquad (15)$$

where the fourth-order tensor $\boldsymbol{I}_{\boldsymbol{C}^{-1}}$ is such that $\boldsymbol{I}_{\boldsymbol{C}^{-1}}:\boldsymbol{A}=\boldsymbol{C}^{-1}\boldsymbol{A}\boldsymbol{C}^{-1}$ for any second-order tensor $\boldsymbol{A}$, in components, e.g. [15]:

$$I_{ABCD}=\frac{1}{2}\Big\{C^{-1}_{AC}\,C^{-1}_{BD}\;+\;C^{-1}_{AD}\,C^{-1}_{BC}\Big\}\;. \qquad (16)$$

3.2. A Saint-Venant-like model

As a second model example, the Saint-Venant-like model is by construction *directly* written with respect to the reference configuration $\mathcal{B}_0$. To do so, we first define a Green-Lagrange-like strain tensor $\tilde{\boldsymbol{e}}$ on the configuration $\boldsymbol{\varphi}_n$ as,

$$\tilde{\boldsymbol{e}} \;=\; \frac{1}{2}\Big\{\tilde{\boldsymbol{c}}-\boldsymbol{1}\Big\}\;, \qquad (17)$$

which, when pull-back to the reference configuration with $\boldsymbol{F}_n$, this gives:

$$\boldsymbol{F}_n^T\,\tilde{\boldsymbol{e}}\,\boldsymbol{F}_n \;=\; \frac{1}{2}\Big(\boldsymbol{C}-\boldsymbol{C}_n\Big) \;\equiv\; \boldsymbol{E}-\boldsymbol{E}_n\;, \qquad (18)$$

where use has been made of relation (9). Let us stress that we refrain from denoting the Green-Lagrange strain tensor difference $\boldsymbol{E}-\boldsymbol{E}_n$ by $\Delta\boldsymbol{E}$, i.e. $\boldsymbol{E}-\boldsymbol{E}_n\neq\Delta\boldsymbol{E}$. This latter is kept for the widely used notation in the literature for the linearization of the Green-Lagrange srain tensor, e.g. relation $(6)_2$.

Next, the second Piola-Kirchhoff stress tensor increment can simply be written as,

$$\Delta\boldsymbol{S}=\lambda(t)\,\big[\big(\boldsymbol{E}-\boldsymbol{E}_n\big):\boldsymbol{1}\big]\,\boldsymbol{1}+2\mu(t)\,\Big(\boldsymbol{E}-\boldsymbol{E}_n\Big)\;, \qquad (19)$$

and, hence, the tangent modulus is then simply given by:

$$\overline{\overline{\boldsymbol{\Xi}}} \;=\; \lambda(t)\,\boldsymbol{1}\otimes\boldsymbol{1}\;+\;2\mu(t)\,\boldsymbol{I}\;, \qquad (20)$$

[2] For the hyperelastic version of the model of Eq. (12), the strain energy function would be $W=\frac{1}{2}\lambda\log^2[J]-\mu\log[J]+\frac{1}{2}\mu(\boldsymbol{C}:\boldsymbol{1}-3)$ in terms of the right Cauchy-Green tensor $\boldsymbol{C}$ and with the state law $\boldsymbol{S}=2\frac{\partial W}{\partial\boldsymbol{C}}$ this gives $\boldsymbol{S}=\lambda\log[J]\boldsymbol{C}^{-1}+\mu(\boldsymbol{1}-\boldsymbol{C}^{-1})$.

where $\boldsymbol{I}$ is the fourth-order unit tensor such that $\boldsymbol{I} : \boldsymbol{A} = \boldsymbol{A}$ for any second-order tensor $\boldsymbol{A}$, in components:

$$I_{ABCD} = \frac{1}{2}\Big\{\delta_{AC}\,\delta_{BD} + \delta_{AD}\,\delta_{BC}\Big\} . \qquad (21)$$

The time-dependent material parameters $\lambda(t)$ and $\mu(t)$ are here again given by Eq. (13).

4. Numerical simulations

For illustrative purposes, we give a set of numerical simulations inspired by the very recent litterature, e.g [8, 13]. We consider straight walls manufactured layer-by-layer at different speeds, each layer with cross-sectional dimensions of 60 mm width and 9.5 mm height. The layers are added step-by-step until divergence of the computational procedure due to structural buckling is observed. To trigger this buckling, we a priori perform a geometrical imperfection by slightly tilting the cross-section of the wall: each layer is tilted about 0.06 mm, i.e. 10^{-3} times the width of one layer. For the fresh concrete, and for all the simulations below, the following time-dependent Young's modulus and a constant Poisson ratio are used:

$$E(t) = 2.94\,t + 25.023\ [\text{kPa}] , \quad \nu = 0.3 , \quad (22)$$

where the time t is here expressed in minutes. For the gravity loading, the reference density is taken as $\rho_0 = 2020\,\text{kg/m}^3$. Here the neoHooke-like incremental model of Section 3.1 is used.

For the finite element simulations, each layer is discretized with isoparametric 8-node hexahedral elements with two elements through the layer thickness, ten elements along its width, and 25 elements each 1 m length, i.e. a total of 500 elements for each layer of 1 m length. Fig. 2 illustrates the initial mesh of a 1 m straight wall with 25 layers.

4.1. A 1 m wall at two different printing speeds

We consider a 1 m printed wall at two printing speeds. As buckling is expected, let make the following assumption: we consider that buckling occurs when the maximum out of plane deformations exceeds half layer-width, i.e. that is when the displacement component v in the Y-direction (see Fig. 2) is such that $v_{\max} \geq 30\,\text{mm}$.

As a first computation, we consider the speed of 0.3 min per layer. The simulations results show that buckling occurs at layer 18 where the maximum out-of-plane displacement is $v_{\max} = 50.2\,\text{mm}$, see Fig. 3(b). We show in Fig. 3(a) the deformed configuration just before buckling: after 17 layers, and where we find that the maximum displacement is $v_{\max} = 7.31\,\text{mm}$. And for illustrative purposed, Fig. 3(c) shows the post-buckling configuration after 19 layers where $v_{\max} = 180.36\,\text{mm}$.

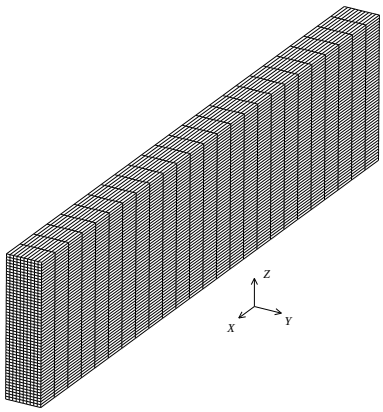

Figure 2: Finite element mesh of a 1 m straight wall with 25 layers. The nodes of the bottom wall are fixed. The layers are activated one by one starting from the bottom during the printing process.

The same computation is now performed at a three times *slower* speed of 0.9 min per layer. The result shows that this time buckling occurs after 22 layers with a $v_{\max} = 49.98\,\text{mm}$. Here again, for illustrative purposes, Fig. 4(a) shows the deformed configurations after 21 layers just before buckling where $v_{\max} = 14.57\,\text{mm}$, and Fig. 4(c) after 24 layers where $v_{\max} = 208.54\,\text{mm}$, i.e. two layers after buckling criterion has been reached.

4.2. A 2 m wall printed concrete

By using the same mesh shown in Fig. 2, we can compute a 2 m printed wall with adequate boundary conditions. Here the face on the (Y, Z)-plane is fixed in the X-direction.

With the same velocity of the printing nozzle as for the 1 m-wall of Fig. 3, this leads to a speed of 0.6 min per layer in the present example. The computation show that in this case, the buckling occurs after 20 layers with a $v_{\max} = 40.38\,\text{mm}$, Fig. 5(b). Here again for illustrative purposes, Fig. 5(a) shows the deformed configurations after 19 layers just before buckling where $v_{\max} = 10.1\,\text{mm}$, and Fig. 5(c) after 21 layers where $v_{\max} = 155.32\,\text{mm}$.

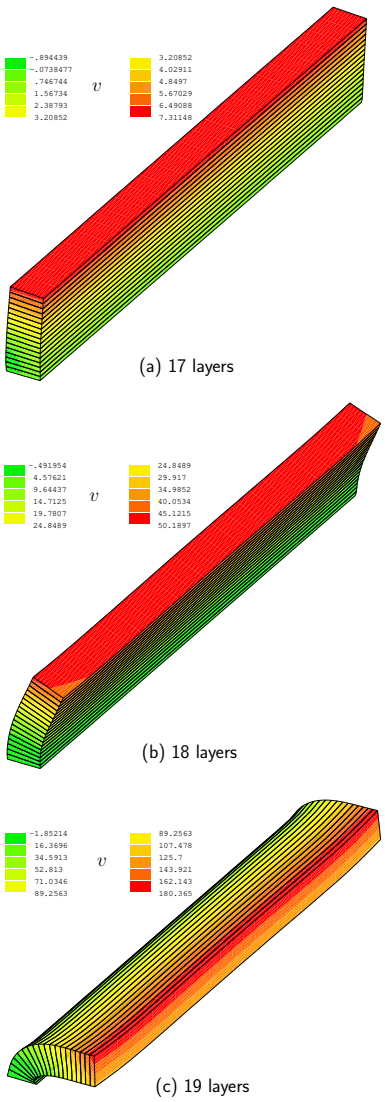

Figure 3: Deformed configurations and displacement field v for the 1 m wall: (a) after 17 layers, (b) after 18 layers and, (c) after 19 layers. Here the printing speed is 0.3 min per layer.

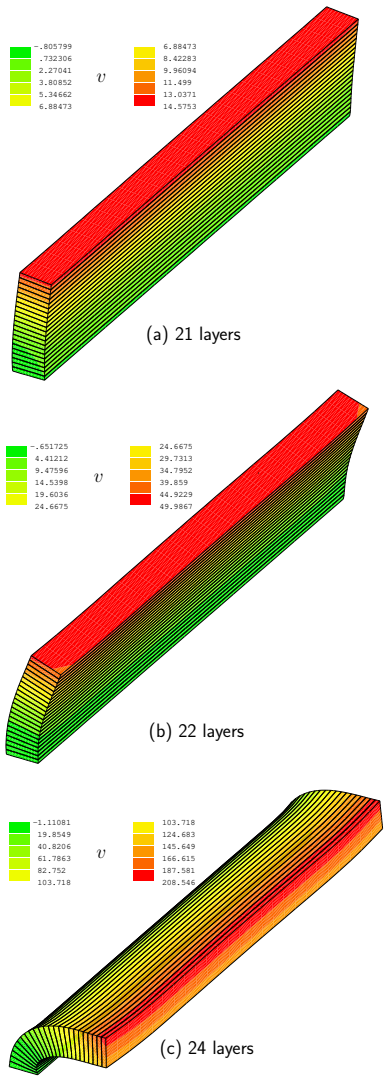

Figure 4: Deformed configurations and displacement field v for the 1 m wall: (a) after 21 layers, (b) after 22 layers and, (c) after 24 layers. Here the printing speed is 0.9 min per layer.

5. Conclusions and perspectives

We have presented a theory for the modelling of the 3D concrete printing problem. The fresh concrete has been described through time-dependent incremental constitutive relations in the finite strain range. As an ingredient, a kinematic choice has been made that is based on the multiplicative decomposition of the deformation gradient. Model examples have been detailed and a set of numerical examples has shown the effectiveness of the proposed framework. In particular, influence of the printing speed on the structural responses can be captured when buckling instability can happen. This latter feature could certainly help the optimization of the printing process.

Further work is still in progress toward more realistic modelling. Among others, the coupling with the hydration of concrete that, in turn, is strongly coupled to the exothermy of the hydration reaction. Furthermore, it goes without saying that the present framework can easily be applied to the man-

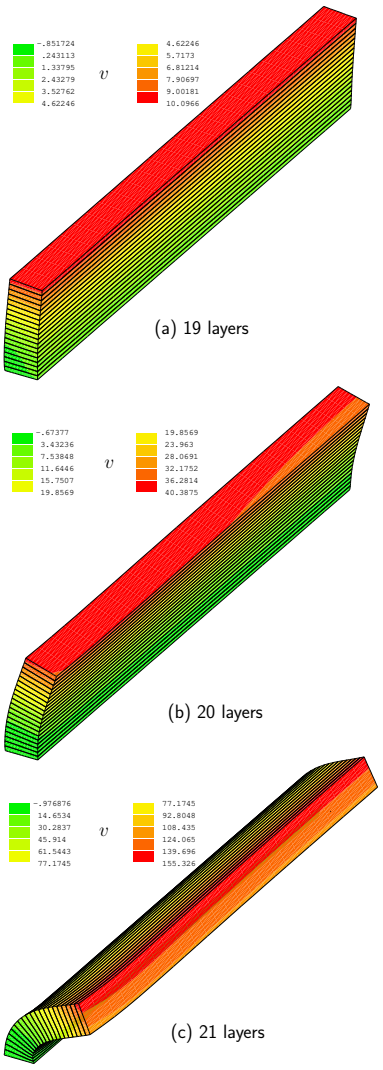

Figure 5: Deformed configurations and displacement field v for the 2 m wall: (a) after 19 layers, (b) after 20 layers and, (c) after 21 layers. Here the printing speed is 0.6 min per layer.

ufacturing of classical 3D printed polymers.

References

[1] S. Lim, R. A. Buswell, T. T. Le, S. A. Austin, A. F. G. Gibb, T. Thorpe, Developments in construction-scale additive manufacturing processes, Automation in Construction **21** (2012) 262–268.

[2] N. Labonnote, A. Ronnquist, B. Manum, P. Rüther, Additive construction: state-of-the-art, challenges and opportunities, Automation in Construction **72**(3) (2016) 347–366.

[3] J. Zhang, J. Wang, S. Dong, B. Han, A review of the current progress and application of 3D printed concrete, Composites Part A **125** (2019) 105533.

[4] B. Panda, J. H. Lim, M. J. Tan, Mechanical properties and deformation behaviour of early age concrete in the context of digital construction, Composites Part B **165** (2019) 563–571.

[5] J. Kruger, S. Zeranka, G. van Zijl, 3D concrete printing: A lower bound analytical model for buildability performance quantification, Automation in Construction **106** (2019) 102904.

[6] S. A. O. Nair, H. Alghamdi, A. Arora, I. Mehdipour, G. Sant, N. Neithalath, Linking fresh paste microstructure, rheology and extrusion characteristics of cementitious binders for 3D printing, Journal of the American Ceramic Society **102** (2019) 3951–3964.

[7] R. J. M. Wolfs, F. P. Bos, T. A. M. Salet, Early age mechanical behaviour of 3D printed concrete: Numerical modelling and experimental testing, Cement and Concrete Research **106** (2018) 103–116.

[8] R. J. M. Wolfs, F. P. Bos, T. A. M. Salet, Triaxial comression testing on early age concrete for numerical analysis of 3D concrete printing, Cement and Concrete Composites **104** (2019) 103344.

[9] G. De Schutter, L. Taerwe, Degree of hydration based description of mechanical properties of early-age concrete, Materials and Structures **29** (1996) 335–344.

[10] Z. P. Bažant, ed., Mathematical modeling of creep and shrinkage of concrete, Wiley, New York, 1988.

[11] A. B. Hauggaard, L. Damkilde, P. F. Hansen, Transitional thermal creep of early age concrete, Journal of Engineering Mechanics **125** (1999) 458–465.

[12] A. S. J. Suiker, Mechanical performance of wall structures in 3D printing processes: Theory, design tools and experiments, International Journal of Mechanical Sciences **137** (2018) 145–170.

[13] R. J. M. Wolfs, A. S. J. Suiker, Structural failure during extrusion-based 3D printinf processes, The International Journal of Advanced Manufacturing Technology **104** (2019) 565–584.

[14] M. P. Serdeczny, R. Comminal, D. B. Pedersen, J. Spangenberg, Experimental validation of a numerical model for the strand shape in material extrusion additive manufacturing, Additive Manufacturing **24** (2018) 145–153.

[15] G. A. Holzapfel, Nonlinear Solid Mechanics. A Continuum Approach for Engineering, John Wiley and Sons, Ltd, Chichester, West Sussex, UK, 2000.

[16] P. Wriggers, Nonlinear Finite Element Methods, Springer-Verlag, Berlin, Heidelberg, 2008.

[17] B. Nedjar, On constitutive models of finite elasticity with possible zero apparent Poisson's ratio, International Journal of Solids and Structures **91** (2016) 72–77.

[18] B. Nedjar, H. Baaser, R. J. Martin, P. Neff, A finite element implementation of the isotropic exponentiated Hencky-logarithmic model and simulation of the eversion of elastic tubes, Computational Mechanics **62**(4) (2018) 635–654.

[19] J. C. Simo, T. J. R. Hughes, Computational Inelasticity, Springer-Verlag, New York, 1998.

[20] J. C. Simo, Numerical analysis and simulation of plasticity, in: P. Ciarlet, J. Lions (Eds.), Handbook of Numerical Analysis, vol. VI, North-Holland, 1998, pp. 183–499.

[21] J. E. Marsden, T. J. R. Hughes, Mathematical foundations of elasticity, Prentice-Hall, Englewood-Cliffs, New Jersey, 1983.